Advances in Applied Mathematics and Mechanics
Adv. Appl. Math. Mech., Vol. **16**, No. 2, pp. 279-304

DOI: 10.4208/aamm.OA-2022-0267
April 2024

A Numerical Study of Integrated Linear Reconstruction for Steady Euler Equations Based on Finite Volume Scheme

Guanghui Hu[1,2], Ruo Li[3] and Xucheng Meng[4,5,*]

[1] *Department of Mathematics & Guangdong-Hong Kong-Macao Joint Laboratory for Data-Driven Fluid Mechanics and Engineering Applications, University of Macau, Macao, China*
[2] *Zhuhai UM Science and Technology Research Institute, Zhuhai, Guangdong 519099, China*
[3] *HEDPS & CAPT, LMAM & School of Mathematical Sciences, Peking University, Beijing 100871, China*
[4] *Research Center for Mathematics, Beijing Normal University, Zhuhai, Guangdong 519087, China*
[5] *BNU-HKBU United International College, Zhuhai, Guangdong 519087, China*

Received 18 October 2022; Accepted (in revised version) 26 January 2023

Abstract. Towards the solution reconstruction, one of the main steps in Godunov type finite volume scheme, a class of integrated linear reconstruction (ILR) methods has been developed recently, from which the advantages such as parameters free and maximum principle preserving can be observed. It is noted that only time-dependent problems are considered in the previous study on ILR, while the steady state problems play an important role in applications such as optimal design of vehicle shape. In this paper, focusing on the steady Euler equations, we will extend the study of ILR to the steady state problems. The numerical framework to solve the steady Euler equations consists of a Newton iteration for the linearization, and a geometric multigrid solver for the derived linear system. It is found that even for a shock free problem, the convergence of residual towards the machine precision can not be obtained by directly using the ILR. With the lack of the differentiability of reconstructed solution as a partial explanation, a simple Laplacian smoothing procedure is introduced in the method as a post-processing technique, which dramatically improves the convergence to steady state. To prevent the numerical oscillations around the discontinuity, an efficient WENO reconstruction based on secondary reconstruction is employed. It is shown that the extra two operations for ILR are very efficient. Several numerical examples are presented to show the effectiveness of the proposed scheme for the steady state problems.

AMS subject classifications: 76M12, 65N08

*Corresponding author.
Emails: huyangemei@gmail.com (G. Hu), rli@math.pku.edu.cn (R. Li), xcmeng@bnu.edu.cn (X. Meng)

Key words: Steady Euler equations, integrated linear reconstruction, finite volume methods, Newton method, WENO reconstruction.

1 Introduction

Steady Euler equations play an important role in aerodynamic shape optimization problems [1,14], and have been viewed as a benchmark problem to evaluate the performance of various numerical schemes in computational fluid dynamics (CFD), see [4,24,37,44,45] among others. A lot of numerical methods have been developed to solve the unsteady and steady Euler equations, e.g., the discontinuous Galerkin method [4,33,50,51], the finite volume method [3,22,36,44], the spectral volume method [47], and the fast sweeping method [11,12].

Nowadays, the second-order finite volume scheme is one of the most popular schemes to solve conservation laws. The second-order finite volume method is a generalization of the classical first-order Godunov's method [24] and mainly includes three steps, i.e., first a piecewise linear polynomial is reconstructed in each cell by using cell averages in the reconstruction patch, then the governing equation is evolved, and finally the cell average is updated in each cell. When the solutions of conservation laws contain discontinuities, how to effectively reduce or prevent spurious oscillations around the discontinuities needs special attention in the reconstruction step. To date, several pioneering works are available in the literature to prevent the numerical oscillations. For example, the total variation diminishing (TVD) [16] limiters have been successfully used for one-dimensional problems to prevent spurious oscillations and to achieve second-order accuracy. However, the implementation of TVD limiter for multi-dimensional problems on unstructured meshes is non-trivial. Moreover, the TVD schemes have been proved to be at most first-order accurate for 2D scalar conservation laws [15]. To overcome these drawbacks, the slope limiters have been introduced to make the numerical solution monotone. The process of slope limiting usually consists of two components, i.e., given the cell averages in the related reconstruction patch of a target cell, the unlimited gradient in this cell is determined by Green-Gauss method [3] or least-squares reconstruction (also known as k-exact reconstruction) [2], and the unlimited gradient is then limited by a certain process to prevent numerical oscillations. On structured meshes, limiters such as the minmod limiter, the Superbee limiter and the van Leer limiter are routinely used to prevent numerical oscillations, and we refer to [24] for the details. On the other hand, the pioneering work of slope limiter on unstructured meshes was due to Barth and Jespersen [3]. It is well known that the non-differentiability of Barth and Jespersen limiter hampers the convergence to steady state [44]. To resolve this issue, the Venkatakrishnan limiter [44] was proposed. However, since the limiter does not preserve strict monotonicity [19,44], slight oscillations can be observed near strong shocks when using this limiter. In order to obtain high-order numerical accuracy and to effectively prevent spurious oscillations, the essentially non-oscillatory (ENO) and the weighted ENO

(WENO) type methods have been successfully implemented on both structured and unstructured meshes, see [17,21,32,41,42,49,54] and the references therein. Compared with ENO schemes, WENO schemes are more robust and are more effective to reach steady states.

Motivated by the work of May and Berger [34], Chen and Li [7] proposed an integrated linear reconstruction (ILR) method, in which the limited gradient in each cell can be directly obtained by solving a linear programming (LP) problem. The advantages of ILR include (i). the reconstruction is completely parameter-free, and (ii). the discrete local maximum principle can be theoretically proved under some mild constraints on grids, and therefore the spurious oscillations around discontinuities can be effectively prevented. However, the geometrical constraints on the grids limit the application of ILR to more general meshes, e.g., the locally refined and highly distorted meshes. To get rid of the constraints on meshes, Chen et al. [6] proposed an improved ILR by imposing constraints on the quadrature points. It is successfully shown in [6] that the improved ILR works very well for the time-dependent hyperbolic conservation laws on arbitrary unstructured meshes. Inherited from ILR, the improved ILR possesses many distinguished features, including (i). the reconstruction is still completely parameter-free, (ii). the discrete local maximum principle can be satisfied on arbitrary unstructured grids, and (iii). when the reconstruction is applied to Euler equations, the finite volume scheme is positivity-preserving [9, 30, 52, 53]. Moreover, an integrated quadratic reconstruction has been proposed in [8] for the 2D and 3D scalar conservation laws. It is noted that only the unsteady conservation laws were considered in [6–8].

In this paper, we numerically study the performance of finite volume scheme using the improved ILR [6] to solve two-dimensional (2D) compressible inviscid steady state Euler equations, and for simplicity, we refer to the improved ILR as ILR hereafter. The numerical framework is based on a Newton-type cell-centered finite volume scheme developed in [18,19,26] for the 2D steady Euler equations. Our numerical results show that the finite volume scheme based on the ILR does not work at all, i.e., the convergence to steady states can not be achieved. In fact, for the one-dimensional case, the ILR reduces to the MC limiter [6], and this limiter is non-differentiable. It is well known that the use of non-smooth slope limiters such as the Barth and Jespersen limiter would hamper the convergence to steady state solution either using the Newton-type or a time-marching method [39, 40, 44]. The ILR also suffers from such a problem, which motivates us to investigate how to apply the ILR method to solve the steady state problems.

The Newton-type finite volume scheme originally developed in [26] mainly consists of two components, including (i). the cell-centered finite volume scheme is used to discretize the governing equations, and the Newton method is adopted to linearize the nonlinear discrete formulation, and (ii). a geometrical multigrid method is utilized to solve the system of linear equations. In the reconstruction step, the ILR proposed by Chen *et. al.* [6] is used to achieve second-order numerical accuracy. To improve the convergence to steady state of 2D Euler equations, a highly efficient gradient smoothing technique is used to obtain averaged gradients of the limited gradients computed by ILR. The tech-

nique used in this paper is the Laplacian smoothing, which has been used in [13] to improve the quality of Delaunay triangulations. In the gradient smoothing procedure, the smoothed gradient in a target cell is an arithmetic average of the limited gradients in cells of its reconstruction patch. It is found that the convergence to steady state can be achieved by using this simple strategy for ILR.

Although the Laplacian smoothing for ILR can significantly improve the convergence to steady state, there is a drawback for this smoothing–the inequality constraints required in the ILR are no longer satisfied, which makes the local maximum principle invalid. As a consequence, slight numerical oscillations would be generated around the discontinuities. To effectively prevent spurious oscillations, the WENO reconstruction is routinely used in the literature, see e.g. [42]. The classical WENO reconstruction needs multiple reconstruction stencils to compute several candidate reconstruction polynomials, and this process is computationally expensive, especially for high-order methods. To partially resolve this issue, an efficient secondary reconstruction is proposed in [29] to provide candidate polynomials. On using the secondary reconstruction, the gradients of candidate linear polynomials can be achieved without additional computational cost when the gradients on all cells are available. In this paper, for the problems containing discontinuities, we adopt the WENO reconstruction based on secondary reconstruction for the linear reconstruction polynomials obtained by ILR with Laplacian smoothing. The numerical results show that the additional computational cost introduced in the WENO reconstruction is low, but the benefits are significant — no numerical oscillations is generated around the discontinuities, and the convergence to steady state can be further accelerated for the problems containing discontinuities.

The rest of this paper is organized as follows. In Section 2, we briefly introduce the inviscid 2D steady Euler equations and the Newton-type finite volume scheme. In Section 3, we first review the basic ingredients for ILR, and then describe the gradient smoothing procedure as well as the WENO reconstruction based on secondary reconstruction. Several numerical examples are presented in Section 4 to show the effectiveness of our method. The conclusion will be given in the last section.

2 Newton-type finite volume method for steady Euler equations

In this section, we first briefly introduce the governing equations, and then present the main steps of Newton-type finite volume scheme, we refer to [19–21, 26] and the references therein for more details.

The 2D steady Euler equations for the compressible inviscid fluid can be written in the following conservative form

$$\nabla \cdot \boldsymbol{F}(\boldsymbol{U}) = \boldsymbol{0}, \tag{2.1}$$

where $\boldsymbol{U}$ and $\boldsymbol{F}(\boldsymbol{U})$ are vectors of the conservative variables and fluxes, respectively, and

they are given by

$$\boldsymbol{U}=\begin{bmatrix}\rho\\ \rho u\\ \rho v\\ E\end{bmatrix} \quad \text{and} \quad \boldsymbol{F}(\boldsymbol{U})=\begin{bmatrix}\rho u & \rho v\\ \rho u^2+p & \rho uv\\ \rho uv & \rho v^2+p\\ u(E+p) & v(E+p)\end{bmatrix},$$

where $(u,v)^\top$, ρ, p, and E denote the velocity, density, pressure, and total energy per unit volume, respectively.

To complete the system, an equation of state is necessary. For a polytropic ideal gas, the equation can be defined by

$$p=(\gamma-1)\left(E-\frac{1}{2}\rho(u^2+v^2)\right),$$

where γ is the ratio of the specific heat coefficients and $\gamma=1.4$ for air.

The Newton-type cell-centered finite volume method originally developed in [26] is employed to discretize the nonlinear governing equations (2.1). The numerical framework of the proposed method mainly consists of two components, i.e., the Newton method is used for linearization of the discrete formulation arising from using cell-centered finite volume method to Eqs. (2.1), and a geometrical multigrid method is adopted to solve the derived linear system. The numerical framework is briefly presented as follows.

Let $\mathcal{T}_h=\{T_i\}_{i=1}^{N_h}$ be a triangulation consisting of triangular cells for the bounded open physical domain $\Omega\subset\mathbb{R}^2$ with boundary $\partial\Omega$, where N_h is the number of cells. Considering the integral form of (2.1) over every cell $T_i\in\mathcal{T}_h$, and using the divergence theorem, we have

$$\int_{T_i}\nabla\cdot\boldsymbol{F}(\boldsymbol{U})\mathrm{d}x\mathrm{d}y=\sum_{j=1}^{3}\int_{e_{ij}}\boldsymbol{F}(\boldsymbol{U})\cdot\boldsymbol{n}_j\mathrm{d}s=\boldsymbol{0},$$

where e_{ij} is the common edge between T_i and its von Neumann neighbor [6] T_j, and $\boldsymbol{n}_j$ is the unit outward normal to edge e_{ij} with respect to T_i.

Replacing the flux $\boldsymbol{F}(\boldsymbol{U})\cdot\boldsymbol{n}_j$ by the numerical flux $\mathcal{F}(\boldsymbol{U}_i,\boldsymbol{U}_j;\boldsymbol{n}_j)$ which is obtained by solving the associated Riemann problem, a fully discrete system is given by

$$\sum_{j=1}^{3}\int_{e_{ij}}\mathcal{F}(\boldsymbol{U}_i,\boldsymbol{U}_j;\boldsymbol{n}_j)\mathrm{d}s=\boldsymbol{0}. \tag{2.2}$$

In the simulation, the Harten-Lax-van Leer-Contact (HLLC) flux [43] is used as the numerical flux.

A linearization mechanism is necessary since the discrete system (2.2) is nonlinear. The Newton iteration method is employed for the linearization, i.e., by setting

$\boldsymbol{U}_i^{(n+1)}=\boldsymbol{U}_i^{(n)}+\Delta\boldsymbol{U}_i^{(n)}$ and keeping the linear terms in the Taylor's expansion, where $\Delta\boldsymbol{U}_i^{(n)}$ is the increment of the conservative variables in the current cell, we obtain the following linearized system

$$\sum_{j=1}^{3}\int_{e_{ij}}\mathcal{F}(\boldsymbol{U}_i^{(n)},\boldsymbol{U}_j^{(n)};\boldsymbol{n}_j)\mathrm{d}s+\sum_{j=1}^{3}\int_{e_{ij}}\frac{\partial\mathcal{F}(\boldsymbol{U}_i^{(n)},\boldsymbol{U}_j^{(n)};\boldsymbol{n}_j)}{\partial\boldsymbol{U}_i^{(n)}}\Delta\boldsymbol{U}_i^{(n)}\mathrm{d}s$$
$$+\sum_{j=1}^{3}\int_{e_{ij}}\frac{\partial\mathcal{F}(\boldsymbol{U}_i^{(n)},\boldsymbol{U}_j^{(n)};\boldsymbol{n}_j)}{\partial\boldsymbol{U}_j^{(n)}}\Delta\boldsymbol{U}_j^{(n)}\mathrm{d}s=\boldsymbol{0}, \tag{2.3}$$

where $\partial\mathcal{F}/\partial\boldsymbol{U}$ denotes the Jacobian matrix of the numerical flux, which can be approximated by numerical differentiation [18]. Since the linearized system (2.3) could be singular, a regularization technique is required. Li et al. [26] used the l_1 norm of cell residual to regularize the system (2.3), that is, the regularized linear system takes the following form

$$\beta\left\|\sum_{j=1}^{3}\int_{e_{ij}}\mathcal{F}(\boldsymbol{U}_i^{(n)},\boldsymbol{U}_j^{(n)};\boldsymbol{n}_j)\mathrm{d}s\right\|_{l_1}\Delta\boldsymbol{U}_i^{(n)}+\sum_{j=1}^{3}\int_{e_{ij}}\frac{\partial\mathcal{F}(\boldsymbol{U}_i^{(n)},\boldsymbol{U}_j^{(n)};\boldsymbol{n}_j)}{\partial\boldsymbol{U}_i^{(n)}}\Delta\boldsymbol{U}_i^{(n)}\mathrm{d}s$$
$$+\sum_{j=1}^{3}\int_{e_{ij}}\frac{\partial\mathcal{F}(\boldsymbol{U}_i^{(n)},\boldsymbol{U}_j^{(n)};\boldsymbol{n}_j)}{\partial\boldsymbol{U}_j^{(n)}}\Delta\boldsymbol{U}_j^{(n)}\mathrm{d}s=-\sum_{j=1}^{3}\int_{e_{ij}}\mathcal{F}(\boldsymbol{U}_i^{(n)},\boldsymbol{U}_j^{(n)};\boldsymbol{n}_j)\mathrm{d}s, \tag{2.4}$$

where $\|\cdot\|_{l_1}$ is the l_1 norm of a vector, and β is a positive parameter, which is set to 2 for all numerical examples.

The advantages of using the l_1 norm of cell residual for the regularization have been demonstrated by many works, and we refer to [18, 20, 21, 26] and the references therein for a detailed discussion. The geometrical multigrid method, see for instance [18, 26], is employed to solve the linear system (2.4) efficiently.

Remark 2.1. In the simulation, the convergence history of the l_∞ norm of total residual, defined by

$$\max_{1\le i\le N_h}\left\|\sum_{j=1}^{3}\int_{e_{ij}}\mathcal{F}(\boldsymbol{U}_i^{(n)},\boldsymbol{U}_j^{(n)};\boldsymbol{n}_{ij})\mathrm{d}s\right\|_{l_1}$$

against the steps of Newton iteration is used to evaluate the performance of the Newton-type finite volume scheme using ILR.

Remark 2.2. The boundary conditions used in the numerical examples include (i) the far field inflow and outflow boundary conditions, and (ii) solid wall boundary condition, i.e., $\boldsymbol{u}\cdot\boldsymbol{n}=0$. The detailed discussion on the treatment of far filed inflow and outflow boundary conditions, including both the subsonic and supersonic cases, can be found in [5]. Furthermore, we refer to the interested reader to [23] for an exhaustive implementation of solid wall boundary conditions.

To obtain the second-order numerical accuracy, the integrated linear reconstruction (ILR) proposed by Chen et al. [6] is used to obtain a linear reconstruction polynomial in each cell, which will be discussed in the next section.

3 Integrated linear reconstruction

In this section, we first briefly review the basic idea of integrated linear reconstruction (ILR), and then introduce the Laplacian smoothing procedure for ILR to improve the convergence to steady state. Finally, we present the efficient WENO reconstruction based on secondary reconstruction to prevent numerical oscillations around the discontinuities.

3.1 A brief review on the ILR

To achieve second-order numerical accuracy, we use the ILR to reconstruct a linear polynomial in each cell. Here, we perform the reconstruction in a component-wise manner. The idea of ILR is briefly described as follows, and we refer to [6] for the details.

Let T_0 be the target cell, and $\{T_i\}_{i=1}^3$ be its von Neumann neighbors, see Fig. 1. The reconstruction patch of T_0 is $\{T_i\}_{i=0}^3$. Furthermore, let (x_i,y_i) and u_i be the barycenter and cell average associated with cell T_i, respectively. We assume that the reconstructed linear polynomial on T_0 is given by

$$R_0(x,y)=u_0+L_x(x-x_0)+L_y(y-y_0),$$

where $\boldsymbol{L}=[L_x,\ L_y]^\top$ is the gradient vector.

The l_2 norm of the error between the values of $R_0(x,y)$ at the barycenters of $\{T_j\}_{j=1}^3$ (the cell averages of R_0 over T_j for $j=1,2,3$) and the related cell averages $\{u_j\}_{j=1}^3$ is used

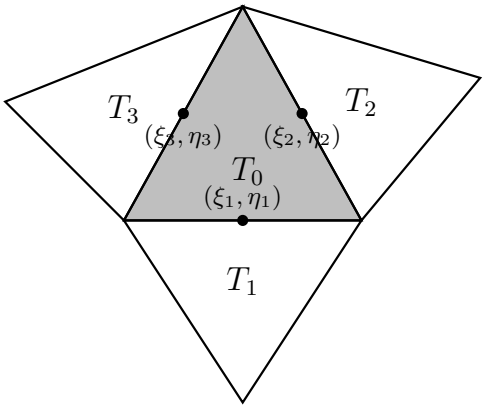

Figure 1: Setup of a reconstruction patch for T_0.

to form the optimization problem, that is, we want to minimize the following objective function

$$\delta(L_x,L_y)=\sum_{j=1}^{3}\big(R_0(x_j,y_j)-u_j\big)^2, \tag{3.1}$$

over all gradients $\boldsymbol{L}=[L_x,\ L_y]^\top$ such that the following constraints on the values of $R_0(x,y)$ at the midpoints (ξ_j,η_j) (see Fig. 1) of the edges of T_0 hold

$$\min\{u_0,u_j\}\le R_0(\xi_j,\eta_j)\le\max\{u_0,u_j\},\quad j=1,2,3. \tag{3.2}$$

Remark 3.1. For the second-order finite volume scheme, the boundary integrals appear in (2.4) can be approximated by the midpoint quadrature rule. Therefore, the midpoints of the edges of T_0 are the quadrature points for the numerical integration of the boundary integrals.

A simple derivation shows that this constrained optimization problem can be transformed into the following double-inequality Quadratic Programming (QP) problem, namely

$$\begin{aligned}&\min_{\boldsymbol{L}}\frac{1}{2}\boldsymbol{L}^\top\mathbf{G}\boldsymbol{L}+\boldsymbol{c}^\top\boldsymbol{L},\\ &\text{s.t. }\ \boldsymbol{b}\le\mathbf{A}\boldsymbol{L}\le\boldsymbol{B},\end{aligned} \tag{3.3}$$

where

$$\mathbf{G}=\sum_{j=1}^{3}\begin{bmatrix}(x_j-x_0)^2 & (x_j-x_0)(y_j-y_0)\\ (x_j-x_0)(y_j-y_0) & (y_j-y_0)^2\end{bmatrix},\quad \boldsymbol{c}=-\sum_{j=1}^{3}\begin{bmatrix}(x_j-x_0)(u_j-u_0)\\ (y_j-y_0)(u_j-u_0)\end{bmatrix},$$
$$\mathbf{A}=\begin{bmatrix}\xi_1-x_0 & \eta_1-y_0\\ \xi_2-x_0 & \eta_2-y_0\\ \xi_3-x_0 & \eta_3-y_0\end{bmatrix},\quad \boldsymbol{b}=\begin{bmatrix}\min\{u_1-u_0,0\}\\ \min\{u_2-u_0,0\}\\ \min\{u_3-u_0,0\}\end{bmatrix},\quad \boldsymbol{B}=\begin{bmatrix}\max\{u_1-u_0,0\}\\ \max\{u_2-u_0,0\}\\ \max\{u_3-u_0,0\}\end{bmatrix}.$$

We refer to [6] for the details. The active-set method is used to solve the constrained QP problem efficiently, see [6] and the references therein for the details.

The above description of ILR is for the interior cells, and the von Neumann neighbors are accurate enough to form the reconstruction patch. However, for the cells located on the boundary of domain, the von Neumann neighbors are not enough to construct the limited gradient. Following [6], when T_0 is a cell lying on the boundary of domain, we use the Moore neighbors to construct the related reconstruction patch, that is, those cells sharing at least one vertex with T_0 would be included in the reconstruction patch, see Fig. 2. Furthermore, the lower and upper bounds for the inequality constraints on the values of reconstructed linear polynomial at the midpoints of edges of T_0 are given by

$$m=\min\{u_0,u_1,\cdots,u_K\}\quad\text{and}\quad M=\max\{u_0,u_1,\cdots,u_K\},$$

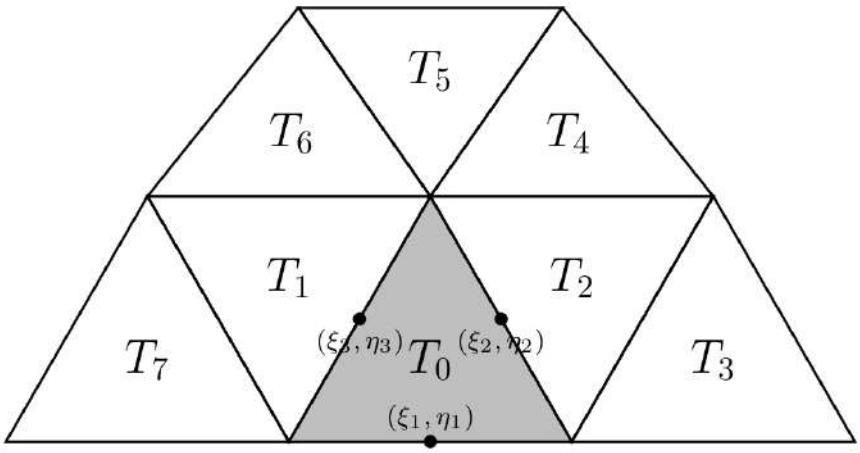

Figure 2: The reconstruction patch for the boundary cell T_0.

respectively, where K is the number of Moore neighbors of the boundary cell T_0.

For the second-order finite volume scheme based on ILR, the limited gradient in each cell can be achieved directly from the constrained optimization problem (3.3). It is proved in [6] that the scheme possesses several excellent properties, including (1). the local maximum principle is satisfied on arbitrary unstructured grids for scalar conservation laws, (2). the reconstruction is parameter-free, and (3). when it is applied to time-dependent Euler equations, the scheme is positivity-preserving. However, the numerical results presented in Section 4 show that the finite volume scheme based on ILR is unable to reach the steady state of Euler equations. This phenomenon is due to the introduction of non-differentiability in the reconstruction function. It is well known that the non-differentiable limiters such as the Barth and Jespersen limiter and the ENO limiter are difficult to obtain the steady state [38]. In the following subsection, we introduce the gradient smoothing for ILR to significantly improve the convergence to steady state.

3.2 A simple smoothing strategy to improve the convergence to steady state

In this work, we use the gradient smoothing to improve the differentiability of reconstruction polynomial obtained by ILR. The gradient smoothing used here is based on the Laplacian smoothing technique [13], which is usually used to improve the quality of a mesh by replacing the selected interior grid point by the weighted average of the points around it. Denote by $\mathcal{P}_0=\{T_0,T_1,T_2,T_3\}$ the reconstruction patch of an interior cell T_0, and let $\boldsymbol{L}_i$ be the limited gradient obtained by ILR on T_i, $i=0,1,2,3$.

Laplacian smoothing (LS) for the gradients obtained by ILR simply uses the arithmetic average of the limited gradients in the reconstruction patch $\mathcal{P}_0$ to replace the lim-

ited gradient on T_0, i.e., if we denote the smoothed gradient on T_0 by $\hat{\boldsymbol{L}}_0$, then

$$\hat{\boldsymbol{L}}_0 = \frac{1}{4}(\boldsymbol{L}_0+\boldsymbol{L}_1+\boldsymbol{L}_2+\boldsymbol{L}_3). \tag{3.4}$$

Similarly, for the cell T_0 lying on the boundary of domain, let $\mathcal{P}_0 = \{T_0, T_1, \ldots, T_K\}$ be the reconstruction patch constructed from the Moore neighbors of T_0, the smoothed gradient on T_0 is

$$\hat{\boldsymbol{L}}_0 = \frac{1}{K+1}(\boldsymbol{L}_0+\boldsymbol{L}_1+\ldots+\boldsymbol{L}_K). \tag{3.5}$$

Example 3.1 (Accuracy test)**.** To show that the ILR with Laplacian smoothing is still of second-order accuracy, in Fig. 3(b), we show the convergence curve of the L_1 norm of error between $u(x,y) = \sin(\pi x)\sin(\pi y)$ and its piecewise linear reconstruction polynomial $u_h(x,y)$ obtained by two different reconstructions: (1). ILR, and (2). ILR with Laplacian smoothing, where the computational domain is $\Omega = [0,1]^2$. In the simulation, six uniformly refined meshes are used, and the coarsest unstructured mesh is presented in Fig. 3(a). It can be observed from Fig. 3(b) that the errors introduced by the two reconstructions are of second-order accuracy, and the numerical accuracy achieved by ILR with Laplacian smoothing is slightly better than that obtained by ILR. In the figure, we also present the L_1 norm of reconstruction errors between the gradient of $u(x,y)$ and the gradient of $u_h(x,y)$, and it can be seen that these errors are of first-order accuracy.

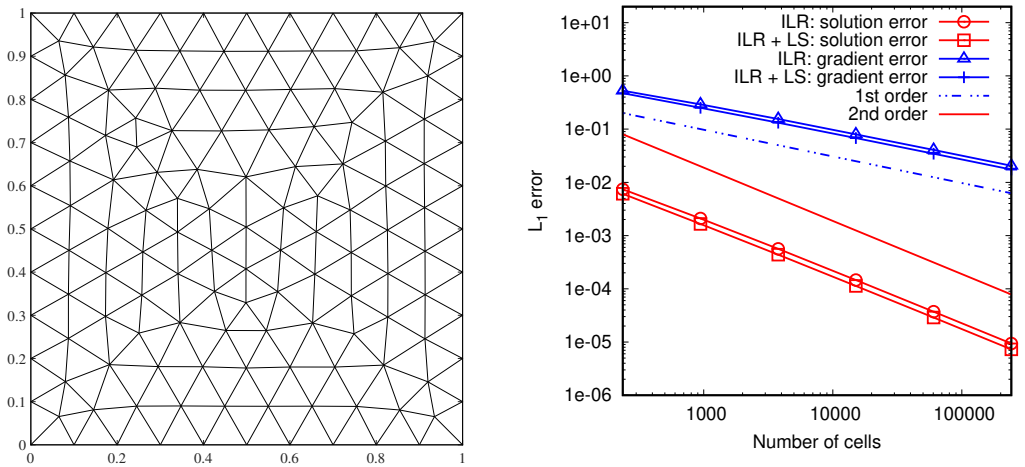

(a) The coarsest unstructured mesh

(b) L_1 error in solution and gradient

Figure 3: The coarsest unstructured mesh, and the L_1 norm of reconstruction errors in solution and gradient on six successively refined meshes using ILR and ILR with Laplacian smoothing (LS).

Example 3.2 (Smoothness test)**.** We next show the effectiveness of the gradient smoothing procedure on improving the smoothness of reconstruction function obtained by ILR. We

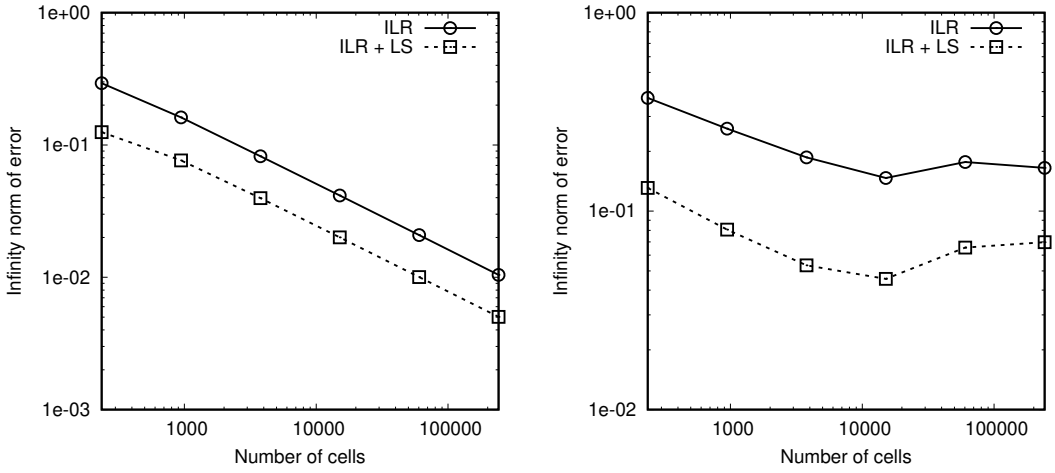

(a) Continuous function (b) Discontinuous function

Figure 4: l_∞ norm of difference in the gradient at the interior edges obtained by ILR and ILR with Laplacian smoothing (LS) for two different functions.

use the l_∞ norm of the difference of the limited or smoothed gradients at interior edges to measure the smoothness of the reconstruction function, that is, we use the l_∞ norm

$$\max_{1\le i\le N_e^{(Int.)}} \int_{e_i} \|\nabla u_{h,e_i}^{(0)} - \nabla u_{h,e_i}^{(1)}\|_{l_1} ds$$

to measure the smoothness, where $N_e^{(Int.)}$ is the number of interior edges of a mesh, e_i is the i-th interior edge, $u_{h,e_i}^{(0)}$ and $u_{h,e_i}^{(1)}$ are the linear reconstruction polynomials in the two cells having e_i as an edge.

In the following, we measure the smoothness of related reconstruction functions for two different functions, where the computational domain and meshes are the ones presented in the last example. The first function is a smooth function given in the previous example, and the second one is a discontinuous function given by

$$g(x,y)=\begin{cases}\sin(\pi x)\sin(\pi y), & \text{if } \ x<0.5,\\ \sin(\pi x)\sin(\pi y)+0.1, & \text{if } \ x\ge 0.5.\end{cases}$$

The result for the smooth function is presented in Fig. 4(a), and that for the discontinuous one is shown in Fig. 4(b). It can be observed from the figure that by using the gradient smoothing technique, the smoothness of the reconstruction function obtained by ILR has been improved.

The numerical results presented in Section 4 show that the Laplacian smoothing for ILR can significantly improve the convergence to steady states. However, there is a po-

tential disadvantage for its use–the inequality constraints (3.2) are no longer valid for the smoothed gradients. As a consequence, spurious oscillations would be generated around the discontinuities since the discrete local maximum principle does not hold any more.

In the following subsection, we will introduce the efficient WENO reconstruction based on secondary reconstruction [29] to prevent spurious oscillations for the problems containing discontinuities.

3.3 WENO reconstruction based on secondary reconstruction

The high-order k-exact WENO finite volume scheme based on the simple and efficient secondary reconstruction is originally proposed by Li and Ren [29] for the time-dependent Euler equations, and has been extended to solve the steady Euler equations in curved geometries [35]. The WENO reconstruction developed in [29] does not need to construct multiple reconstruction stencils to compute several candidate reconstruction polynomials. In [29,35], the classical k-exact reconstruction [2] is performed in every cell to serve as the primary reconstruction, and the additional candidate reconstruction polynomials for the target cell are obtained by secondary reconstruction. The basic idea of secondary reconstruction can be briefly summarized as follows:

The continuations of the k-exact primary reconstructions on neighboring cells of a target cell are served as the additional candidate reconstructions, subjecting to the constraint that the cell average of the continuations should be conserved on the target cell.

The secondary reconstruction for the k-exact WENO finite volume scheme can be easily extended to the case of ILR with Laplacian smoothing, and now the primary reconstruction is the ILR with Laplacian smoothing.

In the following, we describe the implementation of secondary reconstruction in the context of the second-order finite volume scheme, and we refer to [29] for the general cases.

Let T_0 be the target cell, and let $\mathcal{P}_0=\{T_0,T_1,\dots,T_K\}$ be the associated reconstruction patch of T_0. Note that $\mathcal{P}_0$ contains the Moore neighbors of T_0 when T_0 is a cell lying on the boundary of domain. Moreover, let

$$u_i(x,y)=u_i+L_x^{(i)}(x-x_i)+L_y^{(i)}(y-y_i)$$

be the linear reconstruction polynomial obtained by using ILR with Laplacian smoothing in cell $T_i\in\mathcal{P}_0$, where $0\le i\le K$ with $K\ge 3$. The secondary reconstruction polynomial for the cell T_0 obtained by using the primary reconstruction $u_i(x,y)$ on T_i, denoted by $u_{i\to 0}(x,y)$, for $1\le i\le K$, is determined by

$$\begin{aligned}&\frac{\partial^{\boldsymbol{\alpha}}u_{i\to 0}(x,y)}{\partial x^{\alpha_1}\partial y^{\alpha_2}}\Big|_{(x,y)=(x_0,y_0)}=\frac{\partial^{\boldsymbol{\alpha}}u_i(x,y)}{\partial x^{\alpha_1}\partial y^{\alpha_2}}\Big|_{(x,y)=(x_0,y_0)},\\&\forall\boldsymbol{\alpha}=(\alpha_1,\alpha_2)\in\mathbb{N}^2,\quad |\boldsymbol{\alpha}|=\alpha_1+\alpha_2=1,\end{aligned}\tag{3.6}$$

subject to

$$\frac{1}{|T_0|}\int_{T_0} u_{i\to 0}(x,y)\,dxdy = u_0. \tag{3.7}$$

Therefore

$$u_{i\to 0}(x,y) = u_0 + L_x^{(i)}(x-x_0) + L_y^{(i)}(y-y_0), \quad \text{where } 1\le i\le K. \tag{3.8}$$

Now the primary reconstruction polynomial $u_0(x,y)$ and the additional candidate linear reconstruction polynomials $u_{i\to 0}(x,y)$ are available to construct the WENO reconstruction polynomial on T_0, and the construction is described as follows.

Following [17, 19, 21], the smoothness indicator for the linear polynomial $u_{i\to 0}(x,y)$ on the cell T_0 is given by

$$\beta_i = \sum_{|\boldsymbol{\alpha}|=1}\int_{T_0} |T_0|^{|\boldsymbol{\alpha}|-1}\Big(\frac{\partial^{|\boldsymbol{\alpha}|}u_{i\to 0}}{\partial x^{\alpha_1}\partial y^{\alpha_2}}\Big)^2 dxdy = |T_0|\Big((L_x^{(i)})^2 + (L_y^{(i)})^2\Big), \tag{3.9}$$

where $0\le i\le K$, and here $u_{0\to 0}(x,y) := u_0(x,y)$.

The weight ω_i for the candidate linear polynomial $u_{i\to 0}(x,y)$ is determined by

$$\omega_i = \frac{\tilde{\omega}_i}{\sum_{i=0}^{K}\tilde{\omega}_i}, \quad \tilde{\omega}_i = \frac{1}{(\epsilon+\beta_i)^p}, \tag{3.10}$$

where the parameters used in the simulation are $p=2$, and $\epsilon = 10^{-5}$ is a small positive number to avoid division by zero.

Finally, the WENO reconstruction for the cell of interest T_0, denoted by $\tilde{u}_0(x,y)$, is obtained by a convex combination of all candidate linear reconstruction polynomials

$$\tilde{u}_0(x,y) = \sum_{i=0}^{K}\omega_i \cdot u_{i\to 0}(x,y). \tag{3.11}$$

Remark 3.2. In the following, the 1-exact reconstruction using WENO reconstruction based on secondary reconstruction [29] as a limiter is referred to as the linear WENO reconstruction.

4 Numerical examples

In this section, several numerical examples are presented to show the effectiveness of using Laplacian smoothing for ILR to improve the convergence to steady state of 2D Euler equations, and to demonstrate the shock-capturing capability of WENO reconstruction based on the efficient secondary reconstruction. Specifically, the numerical examples presented in Sections 4.1 and 4.2 are concerned with the isentropic smooth flows, and they are used to demonstrate that the ILR with Laplacian smoothing is of second-order accuracy, and to show that the gradient smoothing is necessary to obtain the steady state

even for problems with smooth solutions. In the Section 4.3, we consider transonic flows around a NACA0012 airfoil, which are used to show that the WENO reconstruction is needed to prevent numerical oscillations when the ILR with Laplacian smoothing is applied to problems with discontinuities.

For the following numerical examples, density and velocity of the far field flow are set to be $\rho_\infty = 1$ and $\boldsymbol{v}_\infty = (u_\infty, v_\infty) = (\cos\alpha, \sin\alpha)$, respectively, where α is the angle of attack, and the pressure is $p_\infty = \rho_\infty \|\boldsymbol{v}_\infty\|_2^2/(\gamma M_\infty^2)$, where M_∞ is the Mach number of free-stream flow.

The stop criterion for the Newton method is either the l_∞ norm of total residual (see Remark 2.1) reaches the stop tolerance 10^{-10} or the number of Newton iteration steps reaches 500, unless explicitly stated otherwise. The simulation is performed on a C++ package called AFVM4CFD, and the hardware is a Dell Precision 5530 Mobile Workstation with Intel (R) Xeon (R) E-2176M CPU @ 2.70 GHz and 32 Gb memory.

4.1 Subsonic flow through a channel with a smooth bump

We first consider the inviscid subsonic flow through a channel with a smooth bump [46]. The physical domain is

$$\Omega = \left\{(x,y) \in \mathbb{R}^2 \,|\, -1.5 \le x \le 1.5,\ 0.0625\mathrm{e}^{-25x^2} \le y \le 0.8\right\}.$$

The left boundary is the inflow boundary with the inlet Mach number $M_\infty = 0.5$ and an attack angle $\alpha = 0^\circ$, and the outflow boundary is set at the right boundary, while the wall boundaries are set at the top and bottom boundaries. Since the flow field is isentropic under such a flow condition, we can use the convergence of $L_2(\Omega)$ norm of the entropy error [13,21,23] to evaluate the order of accuracy, and the entropy error is defined by

$$\epsilon_{ent} = \frac{p}{p_\infty}\left(\frac{\rho_\infty}{\rho}\right)^\gamma - 1, \tag{4.1}$$

where p_∞ and ρ_∞ are the pressure and density of the far field flow, respectively.

The coarsest unstructured mesh $\mathcal{T}_h$, see Fig. 5, consists of 574 cells, and five uniformly refined meshes are used in the simulation. We first show the convergence history of l_∞ norm of total residual against the number of Newton iteration steps obtained by ILR in Fig. 6(a), from which we can observe that the steady state can not be obtained on all meshes due to the lack of differentiability of the reconstructed quantities. On the contrary,

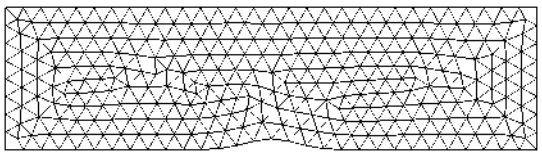

Figure 5: The coarsest unstructured mesh for the simulation of subsonic flow through a smooth bump.

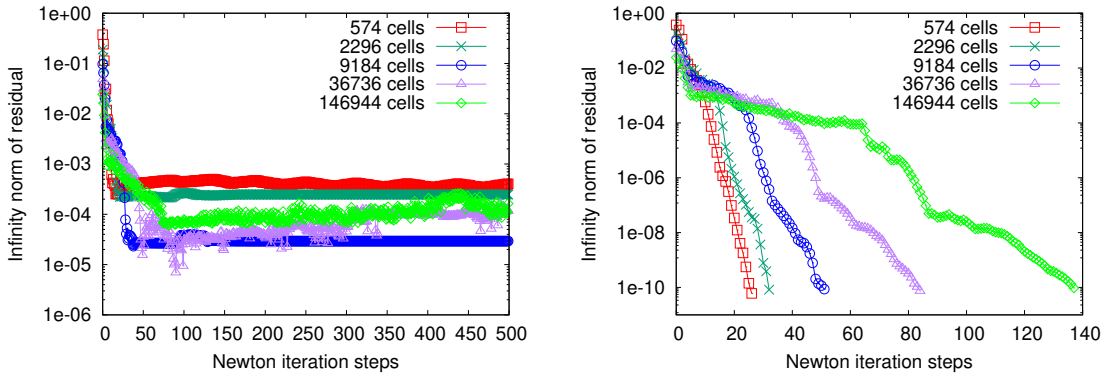

(a) ILR (b) ILR + LS

Figure 6: (Smooth bump) The convergence history of l_∞ norm of total residual on five uniformly refined meshes obtained by (a) ILR, and (b) ILR with Laplacian smoothing (LS).

the residual obtained by ILR with Laplacian smoothing can successfully reach the stop tolerance 10^{-10}, which can be seen from Fig. 6(b). We can conclude from the figure that the gradient smoothing procedure is necessary to reach the steady state when the ILR is used.

We next show the distributions of Mach number isolines obtained by ILR in Fig. 7 (left column), and present those obtained by ILR with Laplacian smoothing in Fig. 7 (right column), where the levels of isolines for the Mach number are uniformly distributed with spacing 0.0195. It can be observed from the figure that (1). the results obtained by ILR with gradient smoothing are more accurate than the results obtained by ILR on the finer meshes, and (2). when the ILR with Laplacian smoothing is used, the distribution of Mach number isolines becomes more symmetric as the baseline mesh is uniformly refined several times, which successfully shows that the method is convergent.

We finally present the $L_2(\Omega)$ norm of entropy errors obtained by using ILR and ILR with Laplacian smoothing in Table 1. In the table, we also report the averaged CPU time (in second) for one Newton iteration step, and show the total number of Newton iteration steps to reach the stop criterion. It can be observed from the table that the second-order accuracy can not be preserved when the ILR is used, this phenomenon can be explained by the fact that the steady state is difficult to achieve when ILR is used. On the contrary, the ILR with gradient smoothing can successfully obtain the optimal convergence rate. Furthermore, we can also see from the table that the averaged CPU time per Newton iteration step for ILR with Laplacian smoothing is only slightly larger than that by using ILR, which shows that the gradient smoothing procedure is not time-consuming at all.

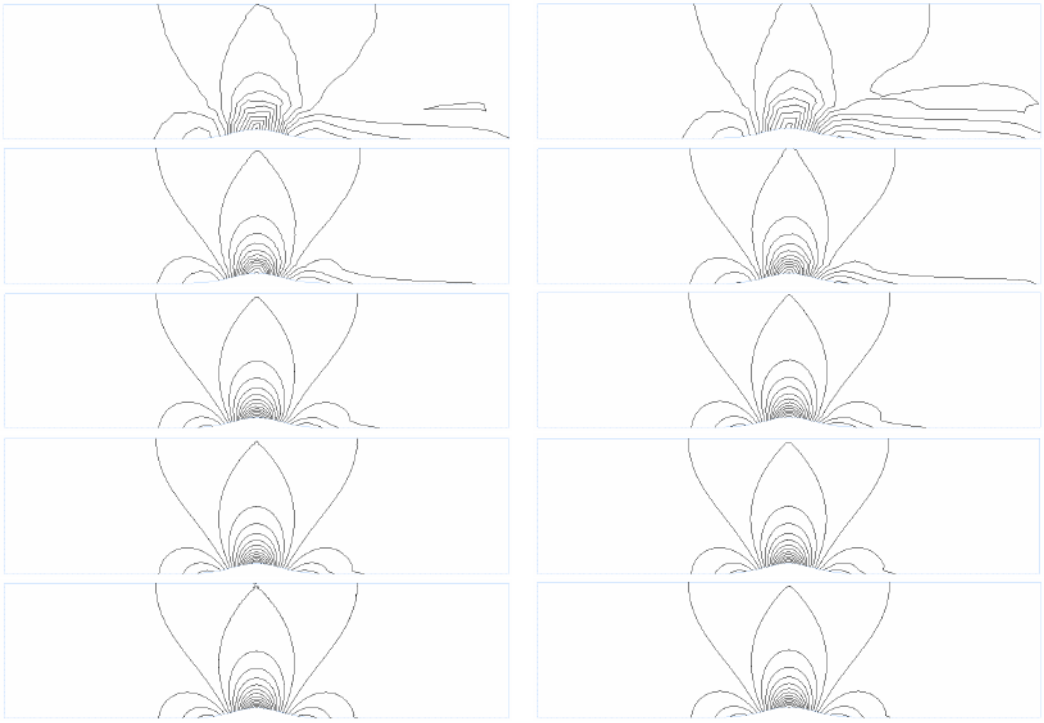

Figure 7: Mach number isolines obtained on five uniformly refined meshes (from top to bottom) using ILR (left column), and ILR with Laplacian smoothing (right column).

Table 1: (Smooth bump). The $L_2(\Omega)$ norm of entropy errors, the related convergence rates, the averaged CPU time per Newton iteration step, and the total number of Newton steps to reach the stop criterion for the Newton type finite volume scheme using ILR and ILR with Laplacian smoothing.

No. of cells	ILR				ILR + LS			
	L_2 Error	Rate	Time per step (s)	No. of steps	L_2 Error	Rate	Time per step (s)	No. of steps
574	2.20e-03	-	0.0197	500	3.39e-03	-	0.0198	27
2296	6.01e-04	1.87	0.0592	500	8.97e-04	1.92	0.0603	33
9184	2.37e-04	1.34	0.215	500	2.39e-04	1.91	0.2243	52
36736	1.11e-04	1.10	0.8779	500	5.38e-05	2.15	0.8804	85
146944	1.54e-04	-0.47	3.676	500	1.23e-05	2.13	3.722	138

4.2 Subsonic flow around a circular cylinder

In this test case, we consider an inviscid subsonic flow of Mach number $M_\infty = 0.38$ with 0° attack angle around a circular cylinder [4]. The detailed setup of this problem can be found in [21]. Similar to the first test case, the flow is isentropic, so we can use the convergence of the $L_2(\Omega)$ norm of entropy errors to evaluate the order of accuracy. In this test case, the maximum number of Newton iteration steps is set to 1000.

In the simulation, the radius of cylinder is $r = 0.5$, and the domain is bounded by an

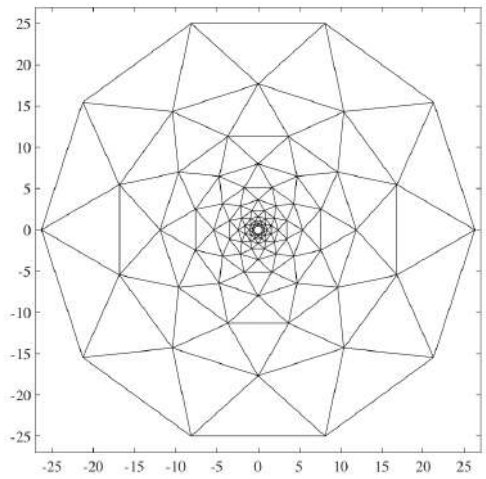

(a) The coarsest mesh: 200 cells

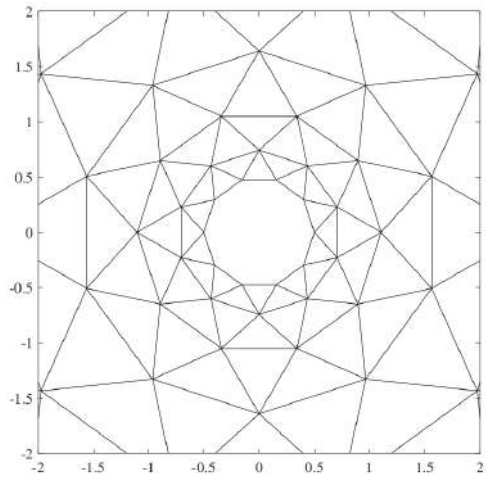

(b) Close-up view of the coarsest mesh around the cylinder

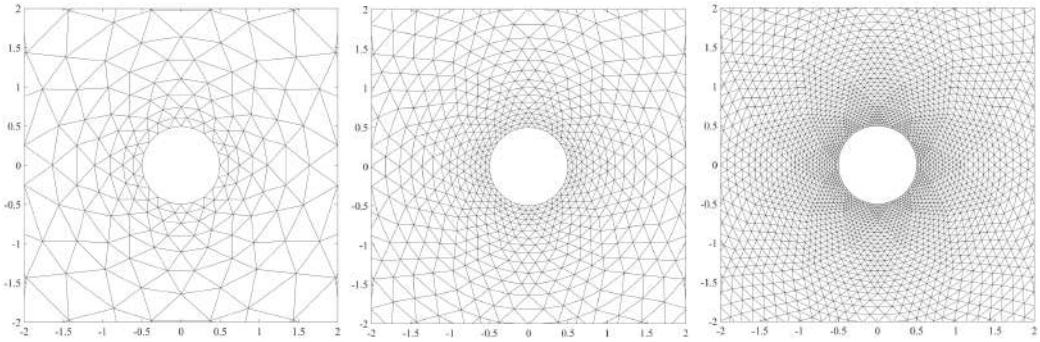

(c) Close-up view of three finer meshes around the cylinder

Figure 8: The meshes used for the simulation of subsonic flow around a circular cylinder.

outer circle with radius $R=26.3$. In Fig. 8(a), we show the coarsest mesh, which contains $10\times10\times2$ cells, and we show the close-up view of the coarsest mesh around the cylinder in Fig. 8(b). In Fig. 8(c), we present the three finer meshes around the cylinder, which are obtained by uniformly refining the coarsest mesh in a body-fitted manner.

The convergence history of l_∞ norm of total residual obtained by ILR on four uniformly refined meshes is shown in Fig. 9(a), and it can be observed that the steady state is not attainable on all meshes. On the contrary, the convergence to steady state can be significantly improved when the gradient smoothing procedure is used for ILR, which can be clearly seen in Fig. 9(b).

We next show the distributions of Mach number isolines obtained from ILR and ILR with Laplacian smoothing in Fig. 10, where the levels of isolines for the Mach number

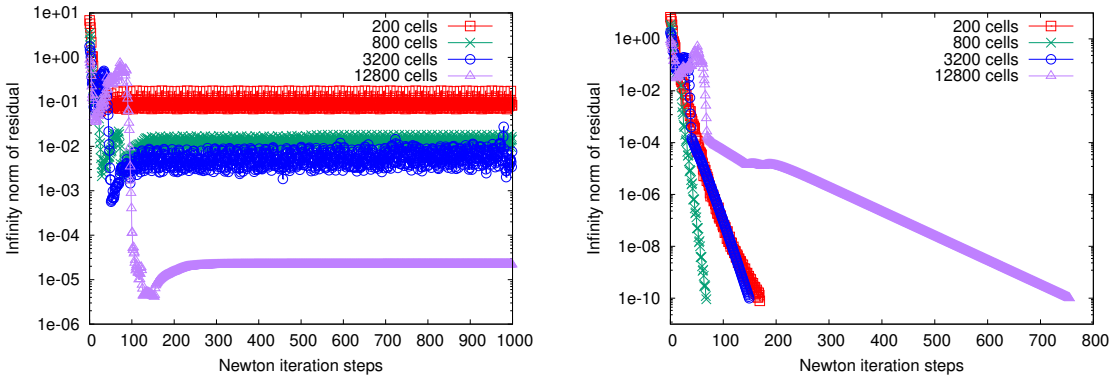

(a) ILR (b) ILR + LS

Figure 9: (Circular cylinder). The convergence history of l_∞ norm of total residual on four uniformly refined meshes obtained by ILR, and ILR with Laplacian smoothing.

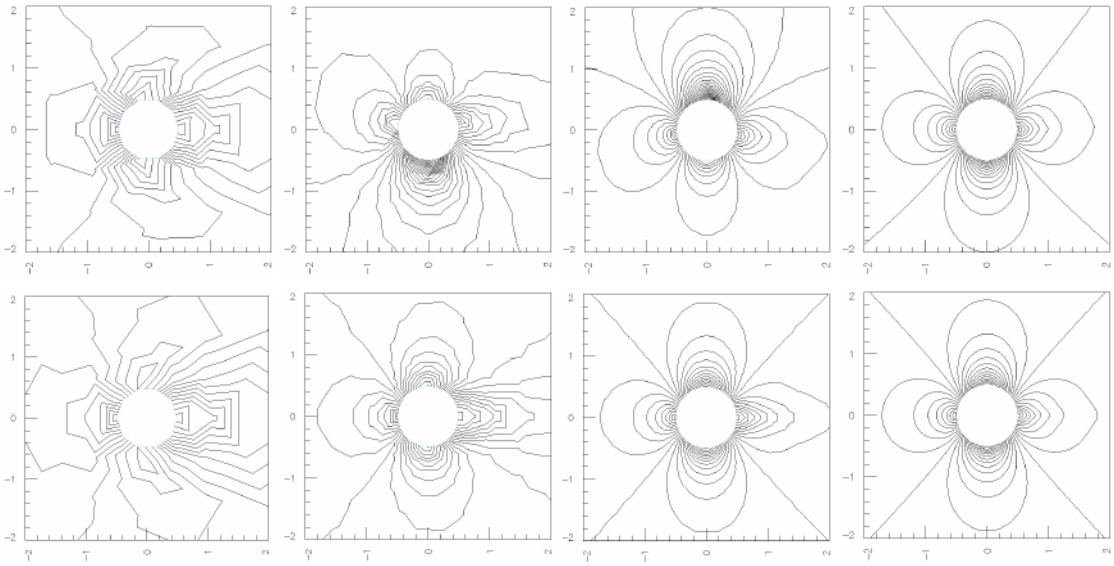

Figure 10: Mach number isolines obtained by ILR (top row) and by ILR with Laplacian smoothing (bottom row) on four successively refined meshes (from left to right).

are uniformly distributed with spacing 0.038. It can be observed from the figure that the results obtained by ILR are unsatisfactory on all meshes, which is explained by the fact that the convergence to steady state can not be achieved by using ILR, while the Mach number contours obtained by ILR with gradient smoothing become more symmetric when the baseline mesh is uniformly refined several times, which demonstrates the convergence of the proposed method.

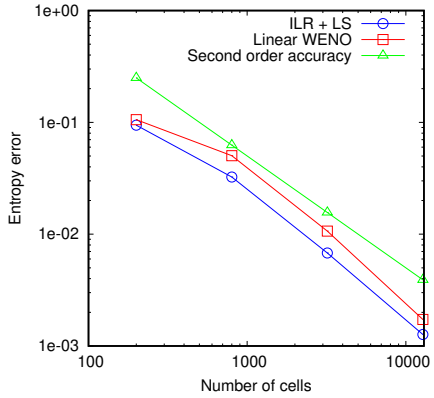

Figure 11: (Circular cylinder). The convergence history of $L_2(\Omega)$ norm of entropy errors.

We finally present the convergence rate of $L_2(\Omega)$ norm of entropy errors obtained by ILR with gradient smoothing in Fig. 11, and as a comparison, we also present the results obtained by the linear WENO finite volume scheme in the figure, where the 1-exact WENO reconstruction based on the secondary reconstruction is used. It can be observed from the figure that the numerical accuracy obtained by ILR with Laplacian smoothing is of second-order accuracy, and the results obtained by ILR with Laplacian smoothing are more accurate than those obtained by linear WENO reconstruction.

4.3 Inviscid transonic flow around a NACA0012 airfoil

In this section, we consider the inviscid transonic flows around a NACA0012 airfoil, and the following two different free-stream flow conditions are considered

(1). Mach number $M_\infty = 0.8$ and attack angle $\alpha = 1.25^\circ$;

(2). Mach number $M_\infty = 0.85$ and attack angle $\alpha = 1^\circ$.

The mathematical expression for the NACA0012 airfoil is

$$y = \pm 0.6(0.2969\sqrt{x} - 0.1260x - 0.3516x^2 + 0.2843x^3 - 0.1036x^4), \quad \text{where} \quad x \in [0,1].$$

The test cases of transonic flow around a NACA0012 airfoil are usually used to evaluate the ability of numerical schemes to prevent numerical oscillations around discontinuities. Although the ILR with gradient smoothing is efficient to achieve the steady state of Euler equations, it would generate numerical oscillations around the discontinuities since the local maximum principle can not be guaranteed any more. Therefore, the numerical examples presented in this section are used to demonstrate that a post-processing of the gradients obtained by ILR with Laplacian smoothing is necessary to achieve oscillations-free numerical results.

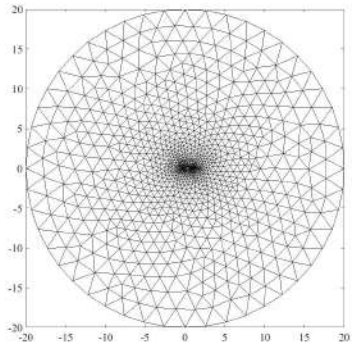

(a) The coarsest mesh

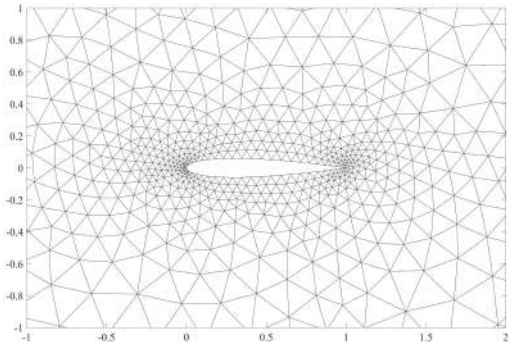

(b) Close-up view of the coarsest mesh around the airfoil

Figure 12: The coarsest mesh used for the simulation of transonic flow around a NACA0012 airfoil.

In the simulation, the physical domain is truncated by an outer circle of radius 20. The coarsest unstructured mesh consists of 2662 triangles, see Fig. 12. Furthermore, in the simulation, two finer meshes are obtained by uniformly refining the coarsest mesh in a body-fitted manner.

We show the convergence history of l_∞ norm of total residual against the Newton iteration steps using ILR for the transonic flow with Mach number $M_\infty=0.8$ at an attack angle $\alpha=1.25^\circ$ in Fig. 13(a), and show the related result for the flow with Mach number $M_\infty=0.85$ at an attack angle $\alpha=1^\circ$ in Fig. 13(d). It can be observed from these two figures that the steady states can not be achieved for these two transonic flow problems on all meshes, just as in the previous test cases. In Figs. 13(b) and (e), we report the convergence history of residual obtained by ILR with the Laplacian smoothing, and it is found that the steady states can be achieved on all meshes, which shows the effectiveness of the use of gradient smoothing to improve the convergence to steady state.

Although the gradient smoothing procedure for ILR can significantly improve the convergence to steady state, this procedure would destroy the inequality constraints on the quadrature points required in ILR, which results in the generation of spurious oscillations around discontinuities. This drawback can be obviously observed from Figs. 14(b) and (e), in which we show the distributions of pressure coefficient along the surface of airfoil for the two different transonic flow problems on the finest mesh using the ILR with Laplacian smoothing procedure, where the pressure coefficient along the airfoil is defined by

$$C_p=\frac{p-p_\infty}{0.5\rho_\infty\|\boldsymbol{v}_\infty\|^2}, \tag{4.2}$$

where p_∞ and $\boldsymbol{v}_\infty=(\cos\alpha,\sin\alpha)$ are the far field pressure and velocity field, respectively. It can be observed from the two figures that there are some slight numerical oscillations around the shocks, while the results obtained by ILR are much better than those obtained

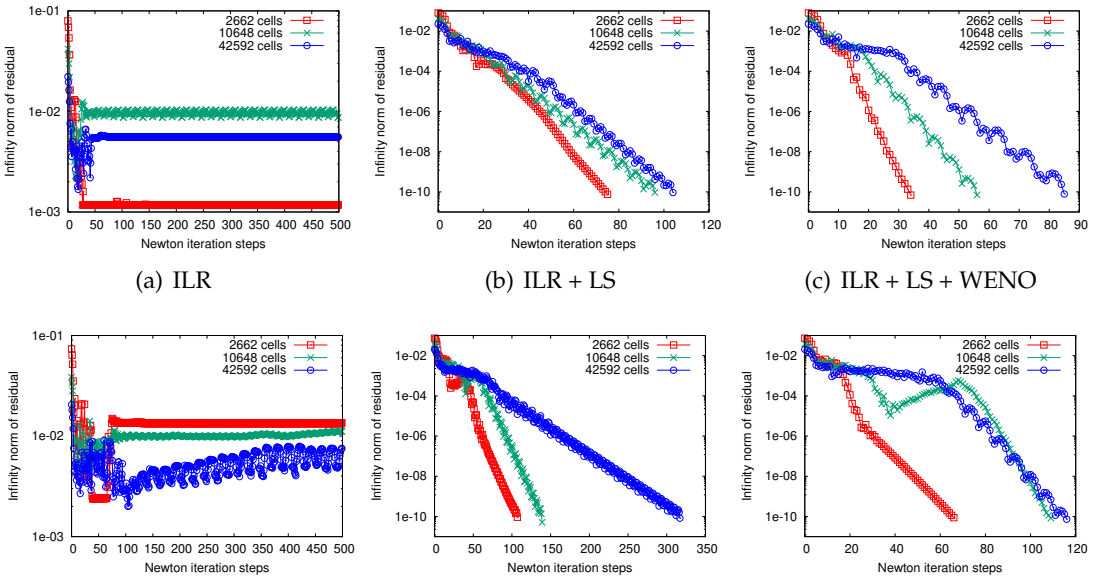

(a) ILR (b) ILR + LS (c) ILR + LS + WENO

(d) ILR (e) ILR + LS (f) ILR + LS + WENO

Figure 13: (NACA0012). The convergence history of total residual for two different transonic flow problems computed on three uniformly refined meshes using three different reconstructions. Top row: $M_\infty=0.8$, $\alpha=1.25^\circ$. Bottom row: $M_\infty=0.85$, $\alpha=1^\circ$.

by ILR with gradient smoothing, see Figs. 14(a), (b) and (d), (e) for the details.

To obtain oscillations-free numerical results, the WENO reconstruction based on secondary reconstruction is used for the limited gradients obtained by ILR with Laplacian smoothing. The related distributions of pressure coefficient along the airfoil on the finest mesh for the two transonic flow problems are shown in Figs. 14(c) and (f), and one can see that there is no numerical oscillations around the shocks. Furthermore, we also show the convergence histories of the l_∞ norm of total residual using ILR with Laplacian smoothing in a combination of WENO reconstruction for the two transonic flow problems in Figs. 13(c) and (f). It can be observed from Fig. 13 that the convergence to steady state of Euler equations has been further improved when the WENO reconstruction is introduced.

In Table 2, we report the averaged CPU time (in second) for one Newton iteration step and the total number of Newton iteration steps to reach the stop criterion for four different reconstructions: (i). the ILR, (ii). the ILR with Laplacian smoothing, (iii). the ILR with both the Laplacian smoothing and WENO reconstruction, and (iv). the linear WENO reconstruction. In the table, we show the results for the two different transonic flow problems on three uniformly refined meshes, where the positive integers corresponding to the column with "#steps" not included in the square brackets represent the related Newton iteration steps to reach the stop criterion for the transonic flow with Mach num-

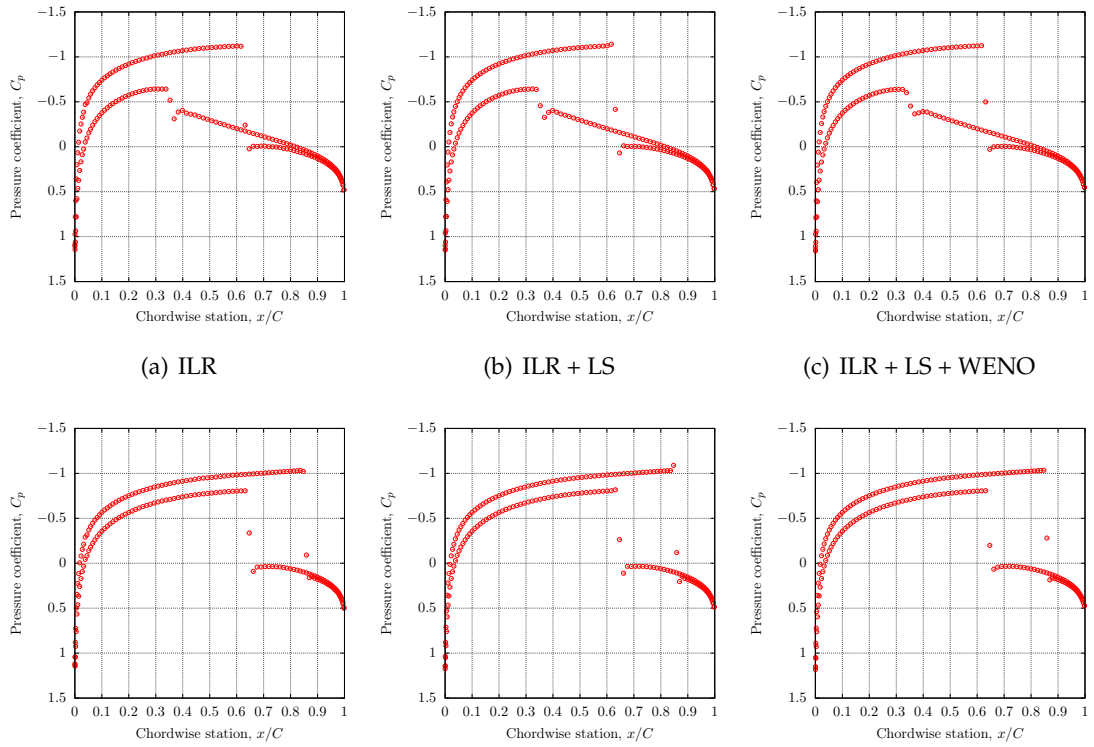

(a) ILR (b) ILR + LS (c) ILR + LS + WENO

(d) ILR (e) ILR + LS (f) ILR + LS + WENO

Figure 14: (NACA0012). Pressure coefficient on the surface of NACA0012 obtained on the finest mesh using three different reconstructions for two transonic flow problems. Top row: $M_\infty=0.8$ and $\alpha=1.25^\circ$. Bottom row: $M_\infty=0.85$ and $\alpha=1^\circ$.

ber $M_\infty=0.8$ at an attack angle $\alpha=1.25^\circ$, while the positive integers in the square brackets correspond to the Newton iteration steps needed for the transonic flow with $M_\infty=0.85$ at an attack angle $\alpha=1^\circ$. It can be observed from the table that (1). for the reconstructions based on ILR, the ILR using Laplacian smoothing in a combination of WENO reconstruction is the most efficient one to reach the steady states on all meshes, (2). the averaged CPU time for one Newton iteration step needed for the ILR using Laplacian smoothing in a combination of WENO reconstruction is about 10% larger than that for ILR, hence the increase of computational cost for the former is not significant, and the former one is very efficient to reach the steady states, and (3). for the four different reconstructions, the ILR using both the Laplacian smoothing and the WENO reconstruction needs the fewest Newton iteration steps to reach the steady states, and the total CPU time it needs is comparable to the time needed by linear WENO reconstruction for the two transonic flow problems on the finest mesh.

Table 2: (NACA0012). The averaged CPU time per Newton iteration step, and the total number of Newton iteration steps to reach the stop criterion using four different reconstructions for two transonic flow problems, where the integers in square brackets represent the total number of Newton iteration steps for flow with $M_\infty = 0.85$ and $\alpha = 1^\circ$, while others correspond to those for the flow of $M_\infty = 0.8$ and $\alpha = 1.25^\circ$.

No. of	ILR		ILR + LS		ILR + LS + WENO		Linear WENO	
cells	Time/step (s)	#steps	Time/step (s)	#steps	Time/step (s)	#steps	Time/step (s)	#steps
2662	0.07188	500 [500]	0.07344	76 [108]	0.07799	35 [67]	0.04299	40 [73]
10648	0.2611	500 [500]	0.2689	97 [140]	0.2809	57 [110]	0.1557	60 [127]
42592	1.0135	500 [500]	1.0625	105 [315]	1.1048	86 [117]	0.6378	142 [192]

5 Conclusions

In this paper, we numerically study the performance an integrated linear reconstruction (ILR) on solving the two-dimensional steady Euler equations. To obtain the convergent results towards the steady state of the system, a highly efficient gradient smoothing procedure based on the Laplacian smoothing is used, and the numerical results show that the convergence to the steady state can be improved significantly. However, the introduction of Laplacian smoothing would destroy the inequality constraints imposed in the construction of ILR, which results in the generation of spurious oscillations around the discontinuities. The efficient WENO reconstruction based on the secondary reconstruction is used to prevent the numerical oscillations, and the increase in computational cost to implement the WENO reconstruction is not significant. The numerical results show that for problems containing shocks, the ILR using both the Laplacian smoothing and WENO reconstruction not only effectively prevents the numerical oscillations, but also significantly improves the convergence to steady states.

Although the ILR with the two post-processing procedures works well for steady state problems containing discontinuities, a better way to apply the ILR to steady state problems should be studied. A possible way is to modify the constraints of optimization problem for ILR such that the modified ILR has excellent steady state convergence as well as the maximum principle preserving property, which will be studied in our future work.

Acknowledgements

The research of Guanghui Hu was partially supported by FDCT of the Macao S.A.R. (0082/2020/A2), National Natural Science Foundation of China (Nos. 11922120 and 11871489), the Multi-Year Research Grant (No. 2020-00265-FST) of University of Macau, and a grant from Department of Science and Technology of Guangdong Province (No. 2020B1212030001). The research of Ruo Li was supported by the National Key R&D Program of China, Project Number 2020YFA0712000. The research of Xucheng Meng is partially supported by the National Natural Science Foundation of China (No. 12101057), the Scientific Research Fund of Beijing Normal University (No. 28704-111032105), and the

Start-up Research Fund from BNU-HKBU United International College (No. R72021112). The authors would also like to thank Dr. Li Chen for helpful discussions during the preparation of this manuscript.

References

[1] W. ANDERSON AND V. VENKATAKRISHNAN, *Aerodynamic design optimization on unstructured grids with a continuous adjoint formulation*, AIAA Paper, (1997), 97-0643.
[2] T. BARTH, *Recent developments in high order k-exact reconstruction on unstructured meshes*, AIAA, 31st, Aerosp. Sci. Meeting Exhibit, (1993).
[3] T. BARTH AND D. JESPERSEN, *The design and application of upwind schemes on unstructured meshes*, AIAA Paper 89-0366, (1989).
[4] F. BASSI AND S. REBAY, *High-order accurate discontinuous finite element solution of the 2D Euler equations*, J. Comput. Phys., 138 (1997), pp. 251–285.
[5] J. BLAZEK, Computational Fluid Dynamics: Principles and Applications, Second edition, Elsevier Science, 2005.
[6] L. CHEN, G. HU, AND R. LI, *Integrated linear reconstruction for finite volume scheme on arbitrary unstructured grids*, Commun. Comput. Phys., 24 (2018), pp. 454–480.
[7] L. CHEN AND R. LI, *An integrated linear reconstruction for finite volume scheme on unstructured grids*, J. Sci. Comput., 68 (2016), pp. 1172–1197.
[8] L. CHEN, R. LI, AND F. YANG, *An integrated quadratic reconstruction for finite volume schemes to scalar conservation laws in multiple dimensions*, CSIAM Trans. Appl. Math., 1 (2020), pp. 491–517.
[9] A. CHRISTLIEB, Y. LIU, Q. TANG, AND Z. XU, *High order parametrized maximum-principle-preserving and positivity-preserving WENO schemes on unstructured meshes*, J. Comput. Phys., 281 (2015), pp. 334–351.
[10] S. CUI, Z. TAO, AND J. ZHU, *A new fifth-order finite volume central weno scheme for hyperbolic conservation laws on staggered meshes*, Adv. Appl. Math. Mech., 14 (2022), pp. 1059–1086.
[11] B. ENGQUIST, B. FROESE, AND Y.-H. TSAI, *Fast sweeping methods for hyperbolic systems of conservation laws at steady state*, J. Comput. Phys., 255 (2013), pp. 316–338.
[12] B. ENGQUIST, B. FROESE, AND Y.-H. TSAI, *Fast sweeping methods for hyperbolic systems of conservation laws at steady state II*, J. Comput. Phys., 286 (2015), pp. 70–86.
[13] D. FIELD, *Laplacian smoothing and Delaunay triangulations*, Commun. Appl. Numer. Methods, 4 (1988), pp. 709–712.
[14] M. GILES AND N. PIERCE, *An introduction to the adjoint approach to design*, Flow Turbul. Combust., 65 (2000), pp. 393–415.
[15] J. GOODMAN AND R. LEVEQUE, *On the accuracy of stable schemes for 2D scalar conservation laws*, Math. Comput., 45 (1985), pp. 15–21.
[16] A. HARTEN, *High resolution schemes for hyperbolic conservation laws*, J. Comput. Phys., 49 (1983), pp. 357–393.
[17] C. HU AND C.-W. SHU, *Weighted essentially non-oscillatory schemes on triangular meshes*, J. Comput. Phys., 150 (1999), pp. 97–127.
[18] G. HU, R. LI, AND T. TANG, *A robust high-order residual distribution type scheme for steady Euler equations on unstructured grids*, J. Comput. Phys., 229 (2010), pp. 1681–1697.
[19] G. HU, R. LI, AND T. TANG, *A robust WENO type finite volume solver for steady Euler equations on unstructured grids*, Commun. Comput. Phys., 9 (2011), pp. 627–648.

[20] G. HU, X. MENG, AND N. YI, *Adjoint-based an adaptive finite volume method for steady Euler equations with non-oscillatory k-exact reconstruction*, Comput. Fluids, 139 (2016), pp. 174–183.
[21] G. HU AND N. YI, *An adaptive finite volume solver for steady Euler equations with non-oscillatory k-exact reconstruction*, J. Comput. Phys., 312 (2016), pp. 235–251.
[22] A. JAMESON, W. SCHMIDT, AND E. TURKEL, *Numerical solution of the Euler equations by finite volume methods using Runge-Kutta time stepping schemes*, 14th Fluid and Plasma Dynamics Conference, (1981).
[23] L. KRIVODONOVA AND M. BERGER, *High-order accurate implementation of solid wall boundary conditions in curved geometries*, J. Comput. Phys., 211 (2006), pp. 492–512.
[24] R. LEVEQUE, *Conservative methods for nonlinear problems*, in Numerical Methods for Conservation Laws, Springer, 1990, pp. 122–135.
[25] J. LI, C.-W. SHU, AND J. QIU, *Moment-Based Multi-Resolution HWENO scheme for hyperbolic conservation laws*, Commun. Comput. Phys., 32 (2022), pp. 364–400.
[26] R. LI, X. WANG, AND W. ZHAO, *A multigrid block LU-SGS algorithm for Euler equations on unstructured grids*, Numer. Math. Theor. Meth. Appl., 1 (2008), pp. 92–112.
[27] R. LI AND W. ZHONG, *A new mapped WENO scheme using order-preserving mapping*, Commun. Comput. Phys., 31 (2022), pp. 548–592.
[28] R. LI AND W. ZHONG, *An efficient mapped WENO scheme using approximate constant mapping*, Numer. Math. Theor. Meth. Appl., 15 (2022), pp. 1–41.
[29] W. LI AND Y.-X. REN, *High-order k-exact WENO finite volume schemes for solving gas dynamic Euler equations on unstructured grids*, Int. J. Numer. Methods Fluids, 70 (2012), pp. 742–763.
[30] J. LIU, J. QIU, M. GOMAN, X. LI, AND M. LIU, *Positivity-preserving Runge-Kutta discontinuous Galerkin method on adaptive Cartesian grid for strong moving shock*, Numer. Math. Theor. Meth. Appl., 9 (2016), pp. 87–110.
[31] Y. LIU, L. YANG, C. SHU, AND H. ZHANG, *A multi-dimensional shock-capturing limiter for high-order least square-based finite difference-finite volume method on unstructured grids*, Adv. Appl. Math. Mech., 13 (2021), pp. 671–700.
[32] Y. LIU AND Y. ZHANG, *A robust reconstruction for unstructured WENO schemes*, J. Sci. Comput., 54 (2013), pp. 603–621.
[33] H. LUO, J. BAUM, AND R. LÖHNER, *On the computation of steady-state compressible flows using a discontinuous Galerkin method*, Int. J. Numer. Methods Eng., 73 (2008), pp. 597–623.
[34] S. MAY AND M. BERGER, *Two-dimensional slope limiters for finite volume schemes on non-coordinate-aligned meshes*, SIAM J. Sci. Comput., 35 (2013), pp. A2163–A2187.
[35] X. MENG, Y. GU, AND G. HU, *A fourth-order unstructured NURBS-enhanced finite volume WENO scheme for steady Euler equations in curved geometries*, Commun. Appl. Math. Comput., 5 (2023), pp. 315–342.
[36] X. MENG AND G. HU, *A NURBS-enhanced finite volume solver for steady Euler equations*, J. Comput. Phys., 359 (2018), pp. 77–92.
[37] X. MENG AND G. HU, *A NURBS-Enhanced Finite Volume Method for Steady Euler Equations with Goal-Oriented h-Adaptivity*, Commun. Comput. Phys., 32 (2022), pp. 490–523.
[38] C. MICHALAK AND C. OLLIVIER-GOOCH, *Accuracy preserving limiter for the high-order accurate solution of the Euler equations*, J. Comput. Phys., 228 (2009), pp. 8693–8711.
[39] K. MICHALAK AND C. OLLIVIER-GOOCH, *Differentiability of slope limiters on unstructured grids*, in Proceedings of Fourteenth Annual Conference of the Computational Fluid Dynamics Society of Canada, 2016.
[40] S. MURMAN, M. BERGER, AND M. AFTOSMIS, *Analysis of slope limiters on irregular grids*, Technical Report NAS-05-007, NAS Technical Report, 2005.

[41] C.-W. SHU, *Essentially non-oscillatory and weighted essentially non-oscillatory schemes for hyperbolic conservation laws*, in Advanced Numerical Approximation of Nonlinear Hyperbolic Equations. Lecture Notes in Mathematics, Vol. 1697, B. Cockburn, C. Johnson, C.-W. Shu, and E. Tadmor, eds., Springer, Berlin, Heidelberg, 1998, pp. 195–285.
[42] C.-W. SHU, *Essentially non-oscillatory and weighted essentially non-oscillatory schemes*, Acta Numer., 29 (2020), pp. 701–762.
[43] E. TORO, M. SPRUCE, AND W. SPEARES, *Restoration of the contact surface in the HLL-Riemann solver*, Shock Waves, 4 (1994), pp. 25–34.
[44] V. VENKATAKRISHNAN, *Convergence to steady-state solutions of the Euler equations on unstructured grids with limiters*, J. Comput. Phys., 118 (1995), pp. 120–130.
[45] Y. WAN AND Y. XIA, *A hybrid WENO scheme for steady-state simulations of Euler equations*, J. Comput. Phys., 463 (2022), 111292.
[46] Z. WANG, K. FIDKOWSKI, R. ABGRALL, F. BASSI, D. CARAENI, A. CARY, H. DECONINCK, R. HARTMANN, K. HILLEWAERT, H. HUYNH, N. KROLL, G. MAY, P.-O. PERSSON, B. VAN LEER, AND M. VISBAL, *High-order CFD methods: current status and perspective*, Int. J. Numer. Methods Fluids, 72 (2013), pp. 811–845.
[47] Z. WANG AND Y. LIU, *Extension of the spectral volume method to high-order boundary representation*, J. Comput. Phys., 211 (2006), pp. 154–178.
[48] Z. WANG, J. ZHU, Y. YANG, L. TIAN, AND N. ZHAO, *A class of robust low dissipation nested multi-resolution WENO schemes for solving hyperbolic conservation laws*, Adv. Appl. Math. Mech., 13 (2021), pp. 1064–1095.
[49] L. WU, Y. ZHANG, S. ZHANG, AND C.-W. SHU, *High order fixed-point sweeping WENO methods for steady state of hyperbolic conservation laws and its convergence study*, Commun. Comput. Phys., 20 (2016), pp. 835–869.
[50] M. ZHANG, W. HUANG, AND J. QIU, *A study on CFL conditions for the DG solution of conservation laws on adaptive moving meshes*, Numer. Math. Theor. Meth. Appl., 16 (2023), pp. 111–139.
[51] W. ZHANG, Y. XING, Y. XIA, AND Y. XU, *High-order positivity-preserving well-balanced discontinuous Galerkin methods for Euler equations with gravitation on unstructured meshes*, Commun. Comput. Phys., 31 (2022), pp. 771–815.
[52] X. ZHANG AND C.-W. SHU, *Positivity-preserving high order finite difference WENO schemes for compressible Euler equations*, J. Comput. Phys., 231 (2012), pp. 2245–2258.
[53] X. ZHANG, Y. XIA, AND C.-W. SHU, *Maximum-principle-satisfying and positivity-preserving high order discontinuous Galerkin schemes for conservation laws on triangular meshes*, J. Sci. Comput., 50 (2012), pp. 29–62.
[54] Y.-T. ZHANG AND C.-W. SHU, *ENO and WENO schemes*, in Handbook of Numerical Methods for Hyperbolic Problems Basic and Fundamental Issues, Vol. 17, R. Abgrall and C.-W. Shu, eds., Handbook of Numerical Analysis, Elsevier, 2016, pp. 103–122.
[55] Z. ZHAO, Y. CHEN, AND J. QIU, *A hybrid WENO method with modified ghost fluid method for compressible two-medium flow problems*, Numer. Math. Theor. Meth. Appl., 14 (2021), pp. 972–997.
[56] J. ZHU, C.-W. SHU, AND J. QIU, *High-order Runge-Kutta discontinuous Galerkin methods with a new type of multi-resolution WENO limiters on tetrahedral meshes*, Commun. Comput. Phys., 29 (2021), pp. 1030–1058.